The International Journal of Advanced Manufacturing Technology (2021) 115:449–462
https://doi.org/10.1007/s00170-021-07188-y

ORIGINAL ARTICLE

# Copper additive manufacturing using MIM feedstock: adjustment of printing, debinding, and sintering parameters for processing dense and defectless parts

Gurminder Singh[1,2] · Jean-Michel Missiaen[2] · Didier Bouvard[2] · Jean-Marc Chaix[2]

Received: 18 December 2020 / Accepted: 30 April 2021 / Published online: 10 May 2021


**Abstract**
In the present study, an additive manufacturing process of copper using extrusion 3D printing, solvent and thermal debinding, and sintering was explored. Extrusion 3D printing of metal injection moulding (MIM) feedstock was used to fabricate green body samples. The printing process was performed with optimized parameters to achieve high green density and low surface roughness. To remove water-soluble polymer, the green body was immersed in water for solvent debinding. The interconnected voids formed during solvent debinding were favorable for removing the backbone polymer from the brown body during thermal debinding. Thermal debinding was performed up to 500 °C, and ~ 6.5% total weight loss of the green sample was estimated. Finally, sintering of the thermally debinded samples was performed at 950, 1000, 1030, and 1050°*C*. The highest sintering temperature provided the highest relative density (94.5%) and isotropic shrinkage. Micro-computed tomography (μCT) examination was performed on green samples and sintered samples, and qualitative and quantitative analysis of the porosity confirmed the benefits of optimized printing conditions for the final microstructure. This work opens up the opportunity for 3D printing and sintering to produce pure copper components with complicated shapes and high density, utilizing raw MIM feedstock as the starting material.

**Keywords** Copper · Extrusion printing · MIM feedstock · Debinding · Sintering · Tomography

## 1 Introduction

The rapidly growing additive manufacturing (AM) processing has simplified the fabrication of complex and customized shapes with different metals [1–4]. The standard AM route involves layer-by-layer consolidation of a metal powder using different energy sources such as laser or electron beam [5–7]. The most popular metal AM techniques are laser beam melting (LBM), electron beam melting (EBM) and direct energy deposition (DED). However, the equipment and manufacturing operations costs are high for these techniques, and the change of material requires many adjustments. Also, laser beam techniques are problematic with high thermal and electrical conductive materials like pure aluminum, copper, or silver owing to reflection of the laser light and heat dissipation. Therefore, less expensive additive manufacturing techniques with more flexible use are still sought after for the mass production of metallic parts.

In the last few years, several researchers have thus explored beamless AM methods for the fabrication of metal parts. Some methods combine polymer 3D printing and other conventional manufacturing processes such as casting, sintering, electroforming, and spraying [8–13]. This opens the way to the fabrication of metal parts at low cost due to less capital investment, less material consumption, and low-skilled worker requirements. These techniques, particularly those involving sintering, are beneficial to materials like copper, challenging to process by LBM and EBM. Owing to the high thermal and electrical conductivities of copper, combined with reasonable mechanical strength, AM-fabricated, complex-shape copper parts may be profitable in various engineering applications, such as actively cooled vehicle skin, power generators, heat exchangers, induction heat coils, radio frequency cathodes, bearings, parts with complex internal cooling channels, and efficient electronic thermal management structures

✉ Gurminder Singh
Gurminder.singh@ucd.ie; Gurmindersingh2012@gmail.com

[1] School of Mechanical & Materials Engineering, University College Dublin, Belfield, Dublin 4, Ireland

[2] CNRS, Grenoble INP, SIMAP, University Grenoble Alpes, 38000 Grenoble, France

[14]. Also, the antimicrobial properties of copper should result in additional applications in the biomedical field.

Among sinter-based AM processes, binder jet printing was reported to allow fabricating pure copper parts. However, a relative density of approximately 80% was obtained after sintering at a temperature as high as 1080 °C by Bay and Williams [15]. Singh and Pandey [16–18] reported a new approach for producing complex copper parts using 3D polymer printing as rapid tooling followed by powder filling and sintering with ultrasonic vibration assistance. This method demonstrated its ability to produce complex components, including overhanging and graded structures. However, once again, the final parts had a low relative density (~ 84%).

Another process consists of extrusion printing of a metal powder-polymer (binder) composite paste followed by removing the polymer (debinding) and the sintering of the powder. Various powders have been tested, such as 17–4 PH [19] and SS 316 [20, 21] steels, zirconia [22, 23], and alumina [24] for the extrusion 3D printing and sintering process by developing metal/ceramic-binder mixture. Also, a few studies have explored extrusion printing of pure copper. In work by Hong et al. [25], the paste (made up of copper, polyvinyl carboxy polymer and poly(vinyl alcohol) PVA) was optimized to ensure good adhesion between the layers during printing with 82 wt.% copper with respect to paste. After sintering the green component at 950 °C for 2 h, a shrinkage of 23% was reported. However, a substantial number of voids remained. Yan et al. [26] also mentioned the manufacture of copper parts by extrusion printing and sintering. A paste with 0.5 μm particle was used. The effects of printing parameters such as layer height, retraction distance, and extrusion volume were investigated to achieve acceptable green parts. After sintering at 1050 °C, 87% relative density with a volumetric shrinkage of ~ 45% has been reported. Zhao et al. [27] have also shown the feasibility of extrusion printing, followed by sintering to produce dense copper products. However, no details on the density, microstructure and other properties of the printed parts have been given. Ren et al. [28] proposed the same technique for extruding copper particles of less than 74 μm size mixed with a binder. A design of experiments was applied to achieve the maximum tensile strength in the green component by adjusting the raster-angle, the layer thickness and the infill degree in the printing process. Furthermore, green samples were sintered close to the melting temperature (1083 °C) to achieve a relative density of ~ 90%, with a high-dimensional reduction of more than 20%. However, several impurities remained in the final products.

The studies described above used composite filaments or paste specially designed and fabricated for printing as raw materials. A more valuable alternative consists of using commercial specially designed MIM feedstocks composed of composite granules. These materials are cheaper because they are produced in large quantities and more effective because they have been designed in terms of binder and metal particle features to provide high-density sintered components. Singh et al. [29] presented a 3D printing method for the fabrication of copper parts by extruding a commercial copper MIM feedstock with a screw extruder as used in the MIM process. Design of experiments-based response surface methodology was used to explore the effect of printing parameters (extrusion temperature, nozzle speed, extrusion flow rate multiplier, and layer thickness) on the green density and the surface roughness of the printed sample. The process parameters were thus optimized to achieve maximum green density (5.5 g/cm$^3$) and minimum surface roughness (1.6 μm). Next, solvent debinding was performed by immersion of the sample in water for 14 h to eliminate water dissolvable binder. The remaining binders were removed by thermal debinding at 1 °C/min up to 500 °C with 1h temperature hold. Sintering was achieved with a two-stage sintering cycle including 4 °C/min heating up to 950 °C, 3 h holding, 4 °C/min heating up to 1030 °C, 3 h holding, 6 °C/min cooling, as proposed in the literature [30]. The sintered samples had a relative density of 91%. This value is lower than the values that have been reported for MIM-shaped parts (95–98%). Therefore, it could likely be increased by further optimizing the process, particularly debinding and sintering. Micro-tomography with a voxel size 5.9 $\mu m$ was used to observe the porosity of both green and sintered materials. The 3D images proved that optimized samples did not exhibit significant printing defects. However, this resolution was certainly not fine enough to allow analyzing all remaining pores.

Therefore, in the present work, as an extension of the work presented in [28], the printing, debinding, and sintering operations were improved to achieve highly dense and low defect copper parts. The novelty of the study was to explore the process parameters in a comprehensive way, so as to obtain sintered copper parts with the maximum density, which could be compared to the value routinely obtained with the MIM process. First, the printing parameters were adjusted to obtain defectless parts with the maximum green density. Next, the solvent and thermal debinding steps were investigated to extract the polymers present in the 3D-printed parts as efficiently as possible. Finally, the sintering cycle was optimized to achieve the highest possible density. Both scanning electron microscopy (SEM) and micro-computed tomography (μCT) analyses were used to disclose the porosity at the surface and in the bulk of the samples, respectively, at different process steps.

## 2 Materials and methods

The different steps for 3D printing and sintering of copper MIM feedstock are shown in Fig. 1. The details of these steps are discussed below.

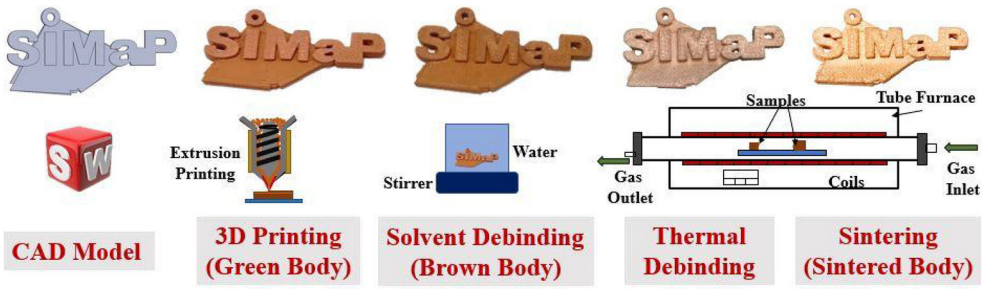


**Fig. 1** Steps for copper part fabrication using MIM feedstock

## 2.1 Materials

Copper MIM feedstock (Cu999 from PolyMIM, Germany) was used as the raw material. This feedstock consists of ~ 3–5 mm granules containing 93.5 wt% of copper and two polymers, namely polyethylene glycol (PEG) and some wax (not precisely specified by the provider). PEG offers flexibility during printing due to its thermoplastic nature. Wax works as the backbone binder to hold the copper particles together after PEG removal. Figure 2 depicts an SEM image of the feedstock and suggests a particle size distribution in the range 2–20 μm for copper particles. Some voids with copper particles and binders in the feedstock granules were also observed. The spherical shape of the particles and their broad size distribution facilitate particle packing in the green body, making it possible to obtain high-density sintered materials [31].

## 2.2 3D printing

3D printing of the green parts was performed with a screw-based extrusion printing machine supplied by AIM3D, Germany. Samples with dimensions up to 255 mm in the three directions can be obtained. As-received feedstock granules were directly fed into the hopper of the machine. A pneumatic controlled piston was used to push the feedstock in the screw extruder and maintain a homogenous flow. A hardened steel nozzle with 0.4 mm diameter was placed at the extruder end for the filament extrusion. A schematic diagram of the machine is given in Fig. 3a. Gcode was generated from the Simplify3D (USA) software for the control of the movement of the printing head. The CAD model for the printing was first generated with SolidWorks software. The CAD model was converted into the tessellation file with the minimum chordal error. Finally, the tessellated file was imported in Simplify3D software for orientation and slicing. Optimization of printing parameters was discussed in a previous paper [29]. The design of an experiment-based approach was used to obtain optimal parameters for maximum green density and minimum surface roughness. The optimal parameters were found to be a layer thickness of 0.05 mm, a nozzle speed of 20 mm/s, an extrusion flow rate of 120% of the standard value, an extrusion temperature of 196°*C*, with a bed temperature of 60°*C*, and an infill density of 100%. Furthermore, extrusion width and overlapping were adjusted in the present work to 0.51 mm and 65% to obtain a higher green density. A printing scan with a closed contour was chosen. The two perimeter contour shells were printed in each layer from outside to inside. A scan raster with a 45° angle offset on each layer was used for the infill pattern. The printing pattern design is displayed in Fig. 3b. For the first layer printing, the nozzle speed was set at 50% of the actual speed for better adhesion to the printing bed. For the present study, cylindrical samples with 8 mm diameter and 4 mm height were fabricated with optimized printing parameters for characterization and subsequent debinding and sintering. A sample with non-optimized, arbitrarily selected parameters (layer thickness 0.2 mm, nozzle speed 60 mm/s, extrusion

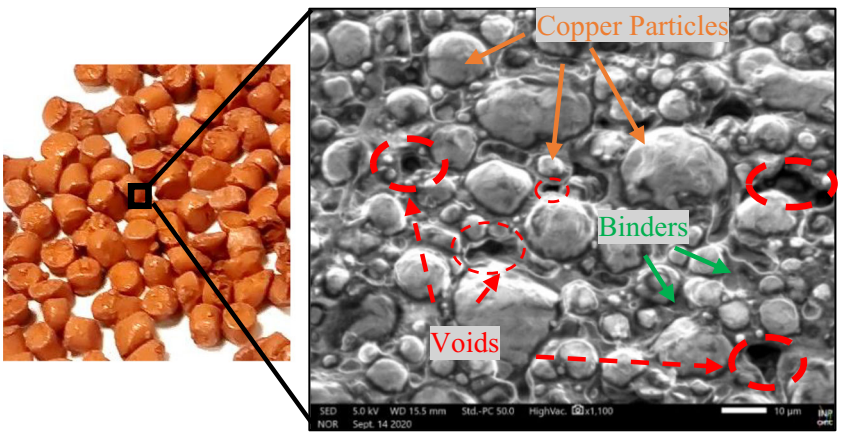


**Fig. 2** SEM image of a copper MIM feedstock granule surface

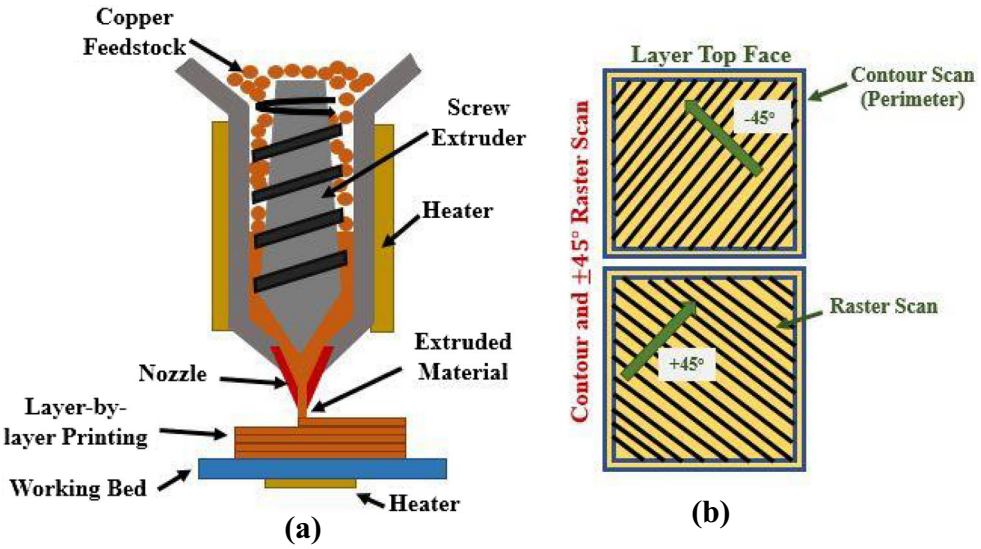


**Fig. 3** **a** Schematic diagram of the extrusion printing process and **b** pattern design for 3D printing

multiplier 100%, extrusion temperature 210 °*C*) was also fabricated to highlight the benefit of the optimization process.

## 2.3 Debinding and sintering

The debinding process was performed in two steps: solvent and thermal debinding, respectively, to remove all binders from the green body. Solvent debinding was performed to extract most of the PEG polymer. The samples were immersed in water with magnetic stirring for 12 h at room temperature, 40 or 60 °*C*. Then, the samples were dried in an oven at 100 °*C* for 2 h. The weight of the samples was measured before and afterwards, and the weight loss was calculated. Thermal and sintering steps were performed in two different tube furnaces to avoid any carbon deposition of binder residue on the sintered sample, which could decrease the density and purity of the sintered copper. The thermal cycles for debinding and sintering are shown in Fig. 4. First, the thermal debinding was performed to remove the backbone binder with a heating cycle of 1 °*C*/min up to 500°*C* and isothermal time of 1 h followed by cooling to room temperature at 4 °*C*/min rate. The thermally debinded samples were placed carefully in the sintering furnace. Sintering was performed by heating at 4 °*C*/min up to 950, 1000, 1030, or 1050 °*C* with a holding time of 3 h and then cooling at 4 °*C*/min to room temperature. The thermal debinding and sintering cycles were performed in He-4%$H_2$ atmosphere.

## 2.4 Characterization

Various characterizations have been employed in the present study to explore the characteristics of the 3D-printed, debinded, and sintered samples. Scanning electron microscopy (SEM) images of cross-sections of the material at different processing steps were taken with a JEOL JSM-IT 500 HR apparatus to study the surface porosity of the samples at different stages of the process. The green density was calculated by measuring the mass and the volume of the printed samples. High green density ensures the lower number of voids in the sample. The mass was determined with an accuracy of 0.001 g, and the volume was deduced from the dimensions measured using a Vernier caliper with an accuracy of 0.01 mm. The surface roughness of the samples in the printing direction was measured using an Olympus DSX500 optical microscope as per the ISO 4287 standard. The surface roughness of the samples was studied to report the quality of the process. The weight density ($\rho$) of the sintered samples was calculated by the 3-mass Archimedes method in air and ethanol. The relative density of the samples was calculated by reporting to the solid copper density (8.96 g/cm$^3$). For mass loss during thermal debinding, thermogravimetric analysis (TGA) was performed in He-4%$H_2$ atmosphere. The experiments and characterizations performed at different stages were carried out three times, and the average and standard deviation were calculated. X-ray diffraction (XRD) analysis was performed using X'Pert Pro MPD from PANalytical to check the purity of the copper sample. The samples were scanned from 25 to 100° angle at 0.97°/min to capture phases with small intensity. For the 3D observation of the samples, microtomography technique was used to capture the porosity of the 3D-printed and sintered samples. Many authors have explored the technique in additive manufacturing and sintering for the evaluation of porosity at different stages [24, 32, 33]. The microtomography machine with a laboratory X-ray source (Easytom XL) was used for the 3D scanning of green and sintered parts. The scan was operated at 150 kV with a voxel size of 5.2 $\mu$m (or 0.93 $\mu$m for a few high-resolution images). In the analysis of tomography results, ImageJ and Avizo Lite software were used. First, the raw μCT files were imported into the ImageJ software. A thresholding operation was

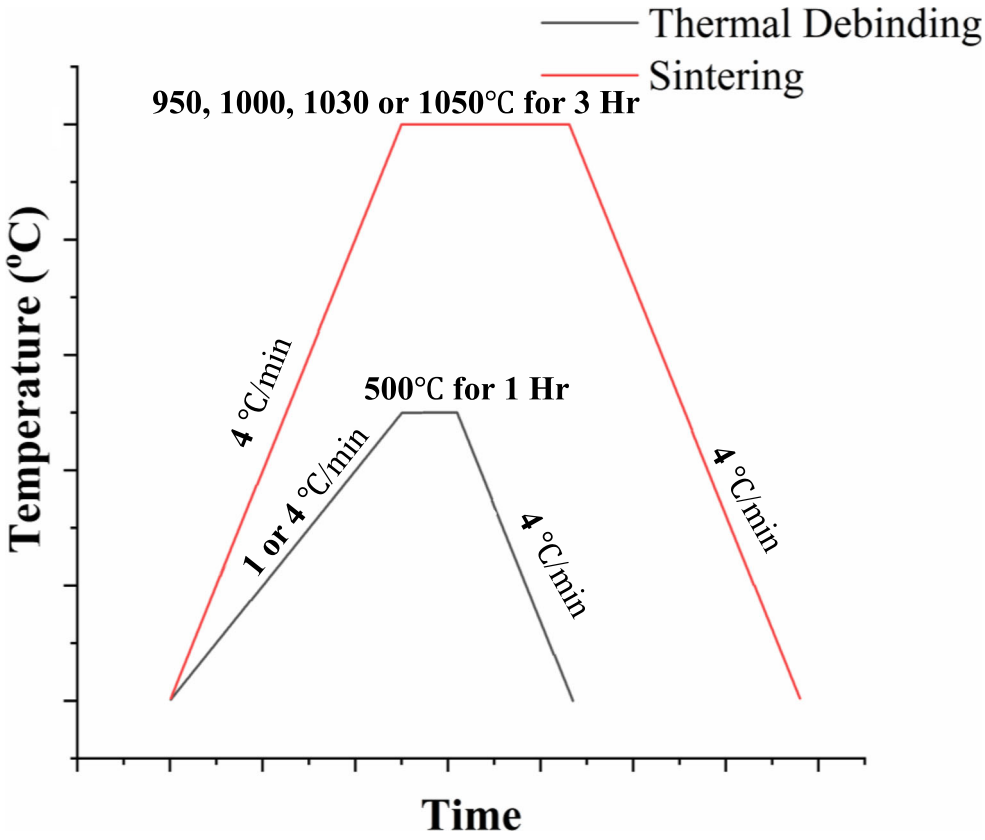


**Fig. 4** Thermal cycles for debinding and sintering

carried out to capture the voids or pores in the samples. The term 'void' is given for the 3D-printed green samples, which contain copper particles and binder and 'pore' for the sintered samples, which only contain copper. After thresholding, the voids/pores were segmented by labeling with 3D connectivity as per the algorithm given by Boulos et al. [34]. The volume ($V$) and surface area ($S_A$) of each void/pore were calculated from the segmented data. The equivalent diameter ($d_{eq}$) and sphericity ($S$) (lying between 0 and 1, where 1 denotes a perfect sphere) were calculated as per Eqs, 1 and 2. Furthermore, the data were imported in the Avizo Lite for visualization of voids or pores in 3D.

$$d_{eq} = 2 \times \left(\frac{3 \times V}{4 \times \pi}\right)^{1/3} \quad (1)$$

$$S = 6 \times V \times \left(\frac{\pi}{S_A{}^3}\right)^{1/2} \quad (2)$$

## 3 Results and discussion

### 3.1 3D printing

The SEM image of the extruded material with the 0.4-mm nozzle is shown in Fig. 5a. Voids larger than the particle size (typically 10–20 μm), named as 'extrusion voids', are observed on the surface of the extruded filament. The melted feedstock is indeed strongly sheared inside the extruder, and the formation of voids may result from the resulting complex state of stress and also from the variation of viscosity as the filament spreads out of the nozzle and solidifies on the deposited layers. Two kinds of voids are observed on the printed green part (Fig. 5b), the 'extrusion voids' already mentioned in the printed filaments and 'printing voids' between the printed layers. Several printing parameters affect the green density during printing. The effect and optimization of significant parameters such as layer thickness, nozzle speed, extrusion multiplier (flow rate), and extrusion temperature were studied for the green density and surface roughness of the sample in a previous study [29]. The optimized results were obtained to be within $5.42 \pm 0.11$ g/cm$^3$ for green density and $3.44 \pm 1.59$ μm for surface roughness. The optimal parameters with furthermore adjustments of overlapping and extrusion width resulted in the fabrication of a green body with a weight density of 5.7 g/cm$^3$ and a surface roughness of 2.12 μm. The green density is thus improved, as compared to the previous study. However, the surface roughness can be varied for the overhang parts, in which the support structure could decrease the surface quality [35]. The SEM image of the sample printed with optimized parameters is shown in Fig. 4b. The sample printed with arbitrary parameters had a weight density of 4.16 g/cm$^3$ and a surface roughness of 26.8 μm. From the weight

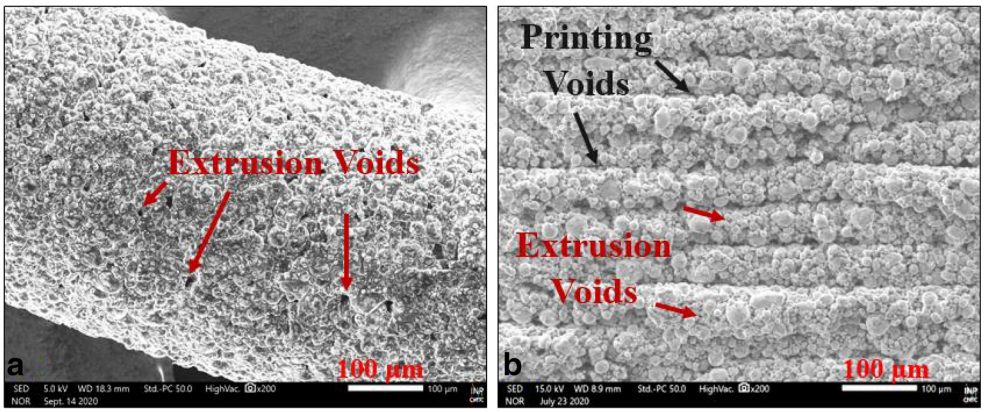


**Fig. 5** SEM image of **a** extruded filament and **b** green part printed with optimized parameters

density of the printed samples and the total weight loss during debinding (see next section), the relative density of copper particle packing with respect to solid copper can be estimated as 60 % and 43 % with optimized and non-optimized parameters, respectively.

To validate the optimized parameters and to study the internal voids of the printing parts, a micro-tomography analysis was performed. 3D renderings of the µCT scans are shown in Fig. 6a, b, for optimized and non-optimized conditions, respectively, with different magnifications. The various phases of the materials, like metal particles, polymers and voids, can be distinguished. Only voids are of interest in the present study. Therefore, the voids were extracted by thresholding and displayed in red color. The volume fraction of voids was calculated as 26% in the non-optimized sample with an average void equivalent diameter of ~ 32 $\mu$m. The frequency of the void diameters for the non-optimized sample is shown in Fig. 6c. For the optimized sample showing much smaller voids (typically < 20 µm) with a volume fraction less than 0.8%, the image contrast and resolution were considered not to be high enough for a relevant calculation of void size distribution. The sample with un-optimized parameters resulted in interconnected voids (they can be easily identified at higher magnification in Fig. 6a) between the layers and large voids in the extruded filaments. On the other side, the sample with optimized parameters resulted in a dense structure with tiny voids.

### 3.2 Solvent and thermal debinding

After printing, the samples were immersed in water for solvent debinding to remove PEG (water-soluble) polymer. Figure 6a depicts the effect of immersion time and temperature on the weight loss of the green body during this step. PEG is almost completely dissolved in water after a few hours of immersion. The dissolution rate increased with increasing temperature. The change in weight loss gets smaller after 10 h. Therefore, to reduce the processing time, a duration of 10 h at 60 °C was selected for experiments. After solvent debinding, the weight loss was ~ 3.8%, and the sample had enough strength to be handled.

Figure 7b, c depicts SEM images of green (3D printed) and brown (solvent debinded) materials. PEG and wax were observed in the green body. Interconnected voids were observed after solvent debinding The interconnected capillary voids could allow the flow of melted backbone polymer and gaseous decomposition products of degradation of the remaining binder harmlessly in a short time [36]. Also, the SEM image in Fig. 7b explains the strength of the sample after solvent debinding. Copper particles are still bonded to each other by the backbone polymer, ensuring interparticle bonds. Similar morphology changes and formation of interconnected voids have been reported in MIM literature [37, 38].

To remove the PEG residue and the remaining backbone polymer, a thermal debinding step was performed. Thanks to the open porosity created by the solvent debinding, the liquid and the gas fumes resulting from the heating of remaining polymers (PEG residues and wax) could escape [39]. A fast-heating rate of 4°*C*/min was first used and resulted in the formation of cracks on the surface, likely due to the rapid flow of melted backbone polymer, which damaged the structure. The heating rate of 1°*C*/min was observed to be an optimal value to perform defect-free thermal debinding. To study the weight loss during thermal debinding, TGA of the solvent debinded sample was performed. Figure 8a depicts the in-situ weight loss during a TGA test. The weight loss from 100 to 300°*C* is attributed to the decomposition of PEG residues remaining after solvent debinding. The sharp weight loss from 300 to 425°*C* is likely due to the removal of the backbone polymer. A total weight loss of 2.7% was observed during thermal debinding. Figure 8b depicts the SEM image of the sample after thermal debinding at 500 °C. The particles were free from any polymer. The total weight loss during solvent and thermal debinding was ~ 6.5%. After these steps, the material had low strength, and it must be handled carefully.

Direct thermal debinding and sintering of a sample without solvent debinding was also tried. However, the high amount of

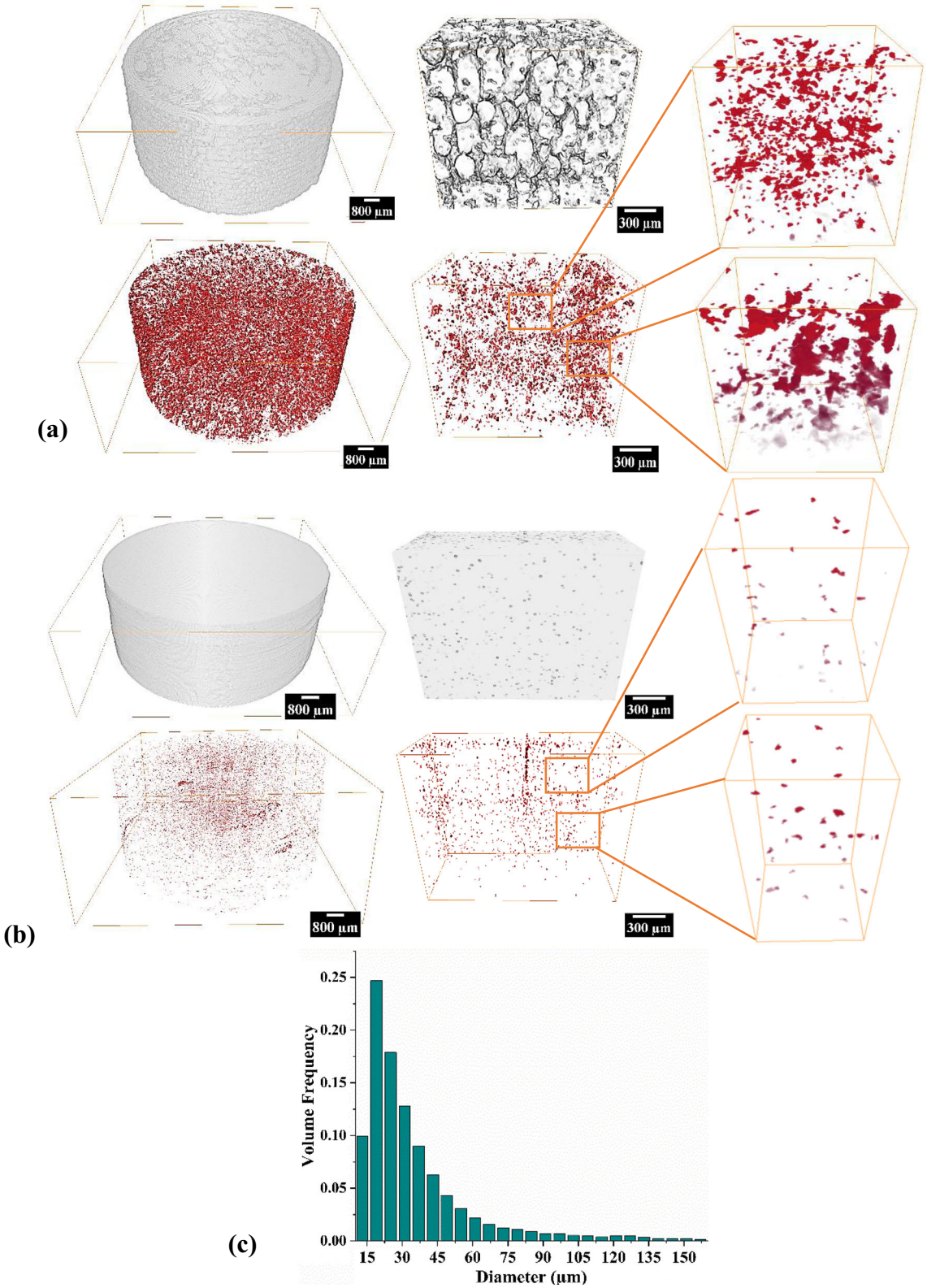


**Fig. 6** 3D volumetric renderings at two different magnifications for (1st row) raw µCT reconstruction and (2nd row) extracted voids by thresholding for green parts printed with **a** non-optimized parameters and **b** optimized parameters, and **c** distribution of void size for non-optimized conditions

polymer to be extracted during thermal debinding resulted in the formation of cracks and in swelling, as shown in Fig. S1. Therefore, solvent debinding is a necessary step for the complete debinding of polymers without any defect formation.

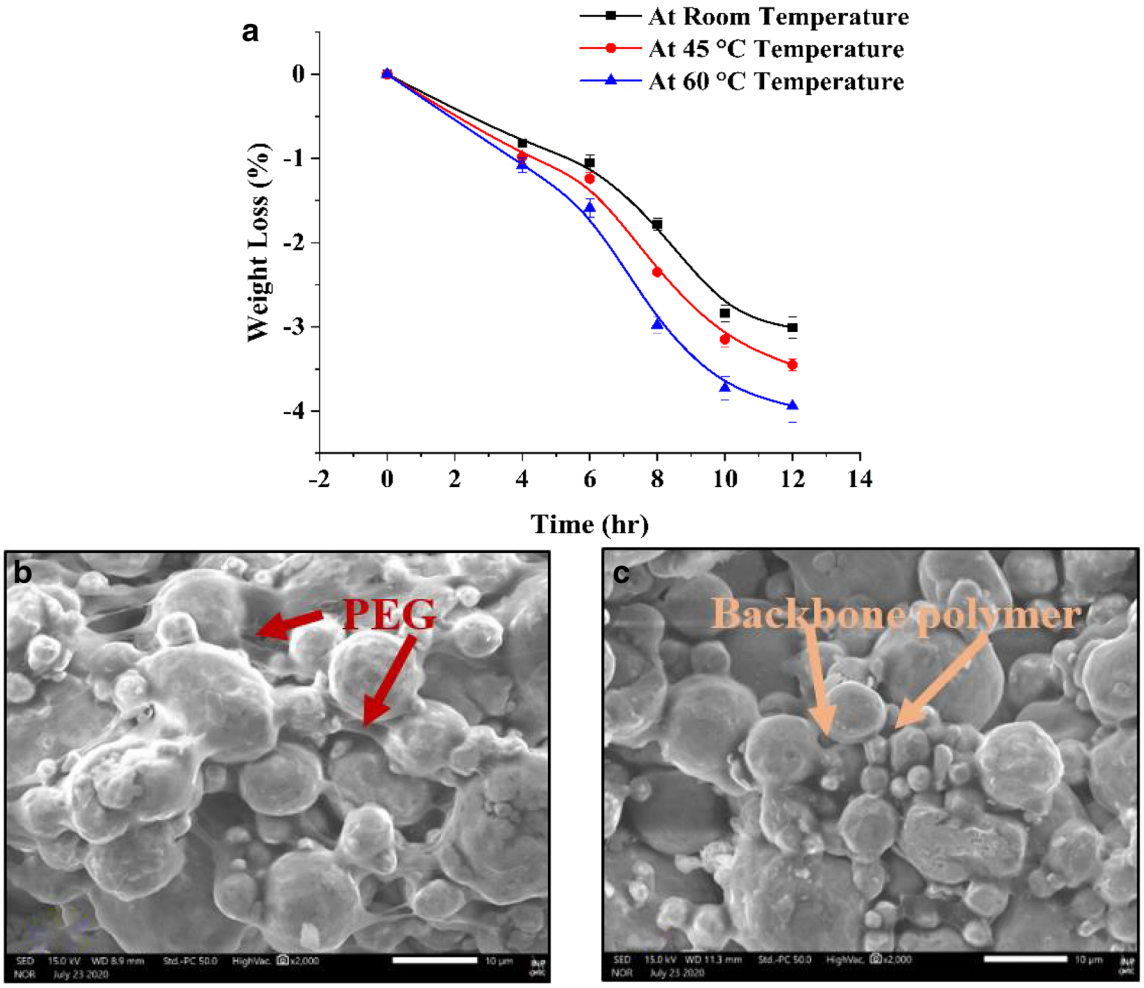


**Fig. 7** **a** Weight loss during solvent debinding, SEM images of **b** green material and **c** brown material

### 3.3 Sintering

After solvent and thermal debinding, sintering was performed for material consolidation and densification. It was carried out in a high flow of He-4%$H_2$ atmosphere to avoid any oxide formation at the particle surface. Sintering is driven by atomic diffusion mechanisms, which are thermally activated [31]. The relative density calculated as per Archimedes' method after sintering at 950, 1000, 1030, and 1050°*C* during 3 h is shown in Fig. 9a. As expected, the density increases with increasing sintering temperature. The maximum relative density of 94.5% was achieved after sintering at 1050 °C for 3 h. Similar behavior of density with respect to sintering temperature was observed by Tang et al. [40] and Singh and Pandey [17].

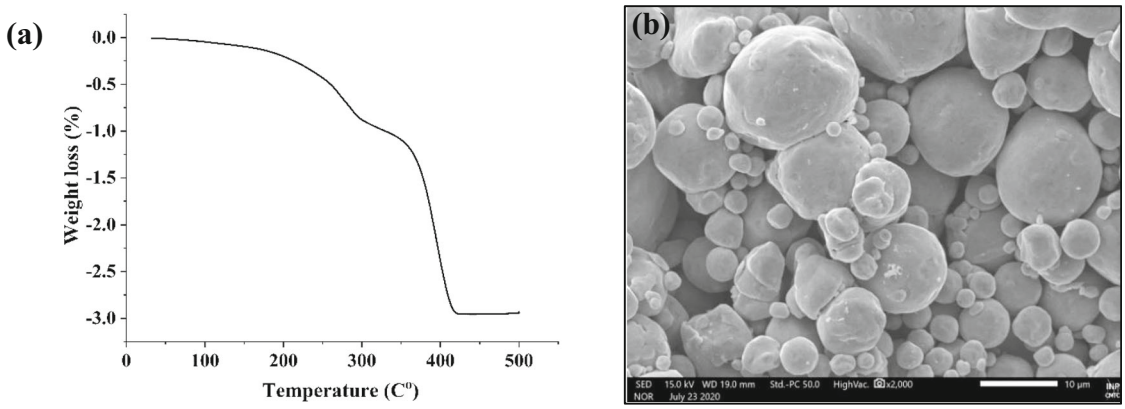


**Fig. 8** **a** Weight loss during thermal debinding and **b** SEM image of the sample after thermal debinding

A few feedstock granules were also sintered with similar debinding and sintering conditions. The resulting relative density was within the standard deviation of the printed samples (Fig. 9a). The residual porosity in sintered samples should then result from incomplete sintering rather than from large extrusion or printing voids which would have been challenging to eliminate. However, the small size of the feedstock granules could have made a bias in the calculation of the density by the Archimedes' method.

The linear shrinkage was also calculated for different sintering temperatures (Fig. 9a). The shrinkage increased with increasing sintering temperature, in accordance with the density increase. The shrinkage was observed to be approximately isotropic. Therefore, compensation of ~ 13.1% in each axis could be added to the CAD model during slicing to get the desired dimensions of the sintered body with high density. Also, the surface roughness of the sintered sample was measured as ~ 2.9 μm. XRD diffraction on the sample sintered at 1050°*C* highlighted pure copper face-centered cubic phase (Fig. 9b). The sintered body was found to be free from any contamination or oxide formation. Figure 9c shows several complex shapes fabricated by the 3D printing method. This shows the efficacy of the process to fabricate pure copper customized parts.

For an in-depth study of porosity, pore size, and pore shape of sintered samples, a μCT analysis was also performed with samples sintered after 3D printing and with sintered feedstock granules. The μCT reconstruction and porosity extraction are shown in Fig. 10. The pores in feedstock granules are observed to be more randomly distributed (see high-magnification image in Fig. 10b) than in the 3D printed part, where the formation of small chains of pores can be seen at certain positions (enlarged image in Fig. 10a), which could be due to the 3D printing defects. The images with 5.2 μm voxel size, i.e., the same order of magnitude as the initial copper particle (5.87 μm), are unable to catch the tiny pores: the porosity calculated with these images is ~ 1.8 and ~ 1.0% for the sintered 3D print body and feedstock granules, respectively, which is much smaller than the one deduced from overall relative density measurement (5.5%). The porosity appears to be mainly constituted by tiny voids, which are below 10 μm. The 3D print sintered sample was machined to 1 mm diameter to enable higher resolution of the μCT scan. The reconstructed body and extracted porosity with low voxel size (0.9 μm) are shown in Fig. 10c. The porosity was calculated as ~ 4.1%, which is close to the value calculated from relative density (5.5%).

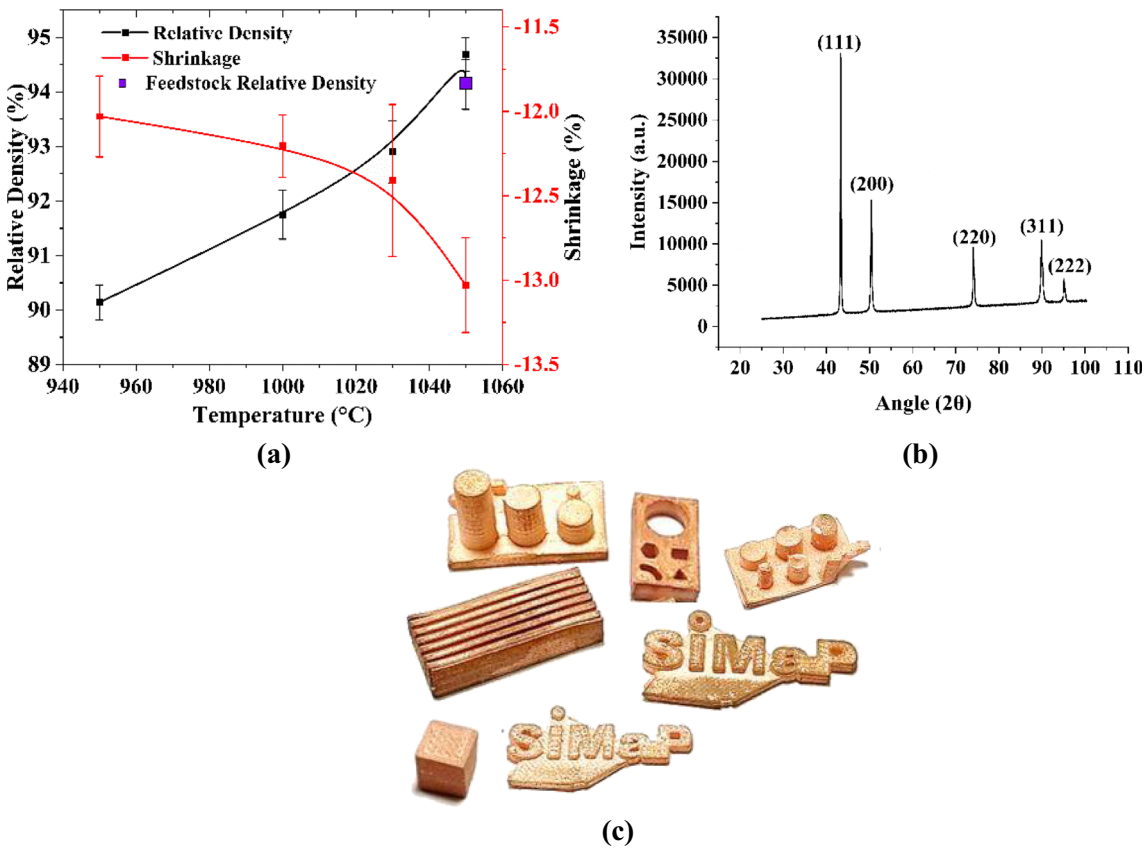


**Fig. 9** **a** Relative density and shrinkage as functions of sintering temperature, **b** XRD pattern of the sintered sample, and **c** different complex shape fabricated by the 3D printing method

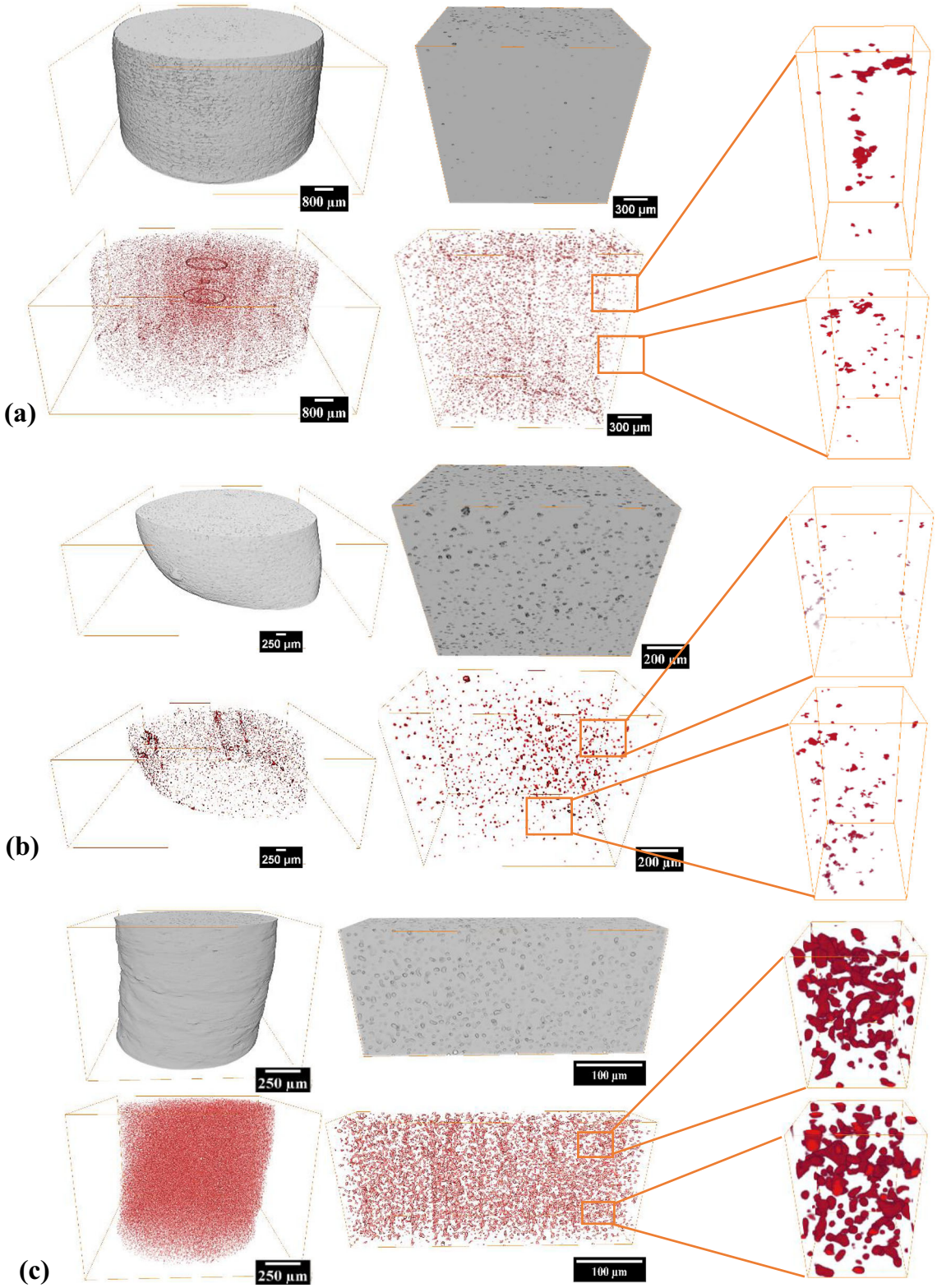


**Fig. 10** 3D volumetric renderings are given at two different scales for (1st row) raw µCT reconstruction and (2nd row) extracted porosity for **a** sintered body and **b** sintered feedstock granules at low resolution (5.2 µm), and **c** sintered body with high resolution (0.9 µm)

Analysis of the size, shape, and orientation of the pores for the sintered body, the sintered feedstock granules, and the sintered body at high resolution is shown in Fig. 11. The average equivalent diameter of large pores, calculated from 5.2 µm resolution images, is ~ 15 $\mu$m for the sintered body. A similar value of ~

16 $\mu$m is obtained for the sintered granules. Figure 11a represents the frequency distribution of the pore diameter in the sintered body and in the sintered granules. The size distributions at low resolution are similar for both materials. A higher fraction of pores more prominent than 25 μm can be observed in the sintered granules. This means that the remaining large pores (> 10 μm) after sintering are not due to the 3D printing, as already assumed from the density values. The average equivalent diameter of pores in the sintered sample at high resolution was calculated to be ~ 7.5 $\mu$m. The higher-resolution image (Fig. 11b) clearly shows that most of the porosities are in the range 3–10 μm, which was not visible in the low-resolution images.

The pore morphology in the sintered body and the feedstock and granules were observed to significantly depart from spherical shape, with a significant contribution in a 0.6–0.8 range of sphericity (Fig. 11c). The small pores captured at high resolution in the sintered body appear to be more spherical, with a significant amount in the 0.75–1 sphericity range. The small pores are isolated or spherical, and characteristics of the final stage of sintering [31].

Figure 11d compares the pore orientation distribution in the sintered body, the sintered feedstock, and the sintered body at high resolution. Each pore orientation is defined as the direction along the ellipsoid's longest axis [41]. The 3D orientation is represented by the angle of altitude (the angle of the orientation vector relative to the vertical axis or direction of the printing). A slight angle of altitude near 0° means that the pores are vertically oriented, whereas a pore that is smooth on the horizontal plane is around 90°. The low-resolution data, which captured the large pores, led to an almost homogeneous distribution of pore orientation in the sintered granules but a significantly larger amount of orientation between 45 and 90° in the sintered printed body. This difference in pore orientation suggests that sintering did not entirely delete the initial local anisotropy of pores introduced by 3D printing. It could also be due to the rearrangement of the particles in the 3D printed sample during the sintering process. In the high-resolution image, where the number of tiny pores is much larger, a homogeneous distribution of orientations is observed, which indicates that the 3D printing process does not influence the final minor porosity.

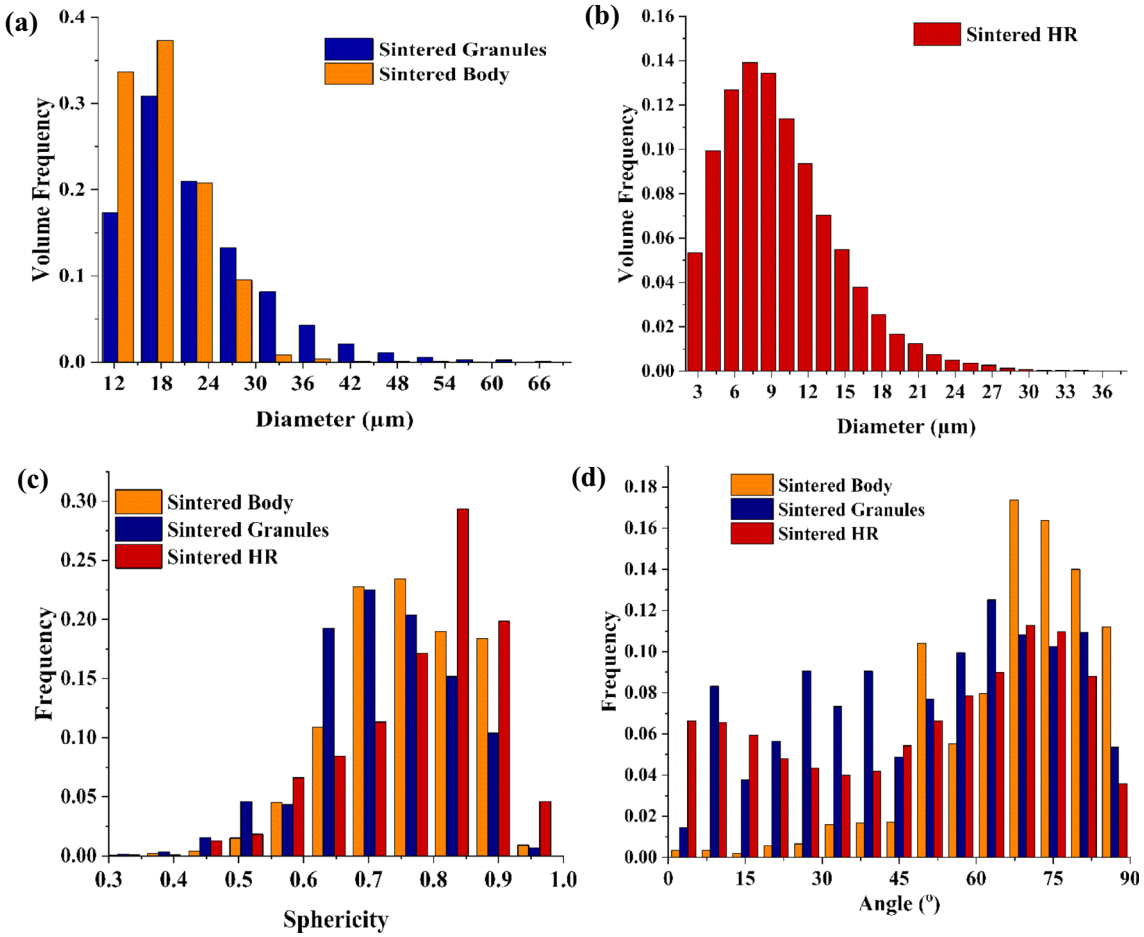


**Fig. 11** Frequency of the voids with regard to **a**, **b** volume, **c** sphericity, and **d** principal axis angle for the sintered body, sintered feedstock granules, and sintered body at high resolution (HR)

## 4 Conclusions

The 3D metal printing and sintering of dense copper starting with metal injection moulding raw material was studied. 3D extrusion printing, solvent and thermal debinding, and sintering steps were performed to achieve copper samples with high relative density and minimal defects. The major conclusions are given below:

1. Green samples fabricated using extrusion 3D printing with optimized printing parameters resulted in a green density as high as 5.7 g/cm$^3$ (~ 60% relative density). Such optimization is absolutely required since a sample fabricated with non-optimized parameters showed a much lower value as a consequence of large voids formed during printing.
2. A maximum weight loss of ~ 3.8% during solvent debinding was observed after 10 h of immersion in water at 60°*C*. After solvent debinding, the remaining unsoluble backbone polymer gave enough strength to the sample for further handling. The interconnected voids formed during solvent debinding acted as transport channels for the removal of backbone polymer during thermal debinding, which was evaporated at 425°*C*. The total weight reduction in the samples after debinding was ~ 6.5%.
3. A high densification was obtained after sintering at 1050 °C for 3 h, with ~ 94.5% relative density and ~ 13.1% isotropic shrinkage. XRD analysis confirmed the purity of the sintered sample, which was free from any oxidation. The sintered raw feedstock granules resulted in similar relative density as compared to the 3D printed part. Therefore, the remaining porosity is not due to 3D printing voids, but results from an intrinsic sintering limitation of the feedstock powder (initial copper density due to the volume occupied by the polymer). Microtomography analyses at high resolution of the sintered sample showed spheroidal pores with a size distribution in the micron range.
4. Pure copper parts with 94.5% relative density were thus obtained by 3D extrusion printing and sintering after optimizing the different steps of the process. This result is better than the ones reported in the literature for the fabrication of copper components by 3D printing and sintering combination, such as ~ 83.9% by rapid tooling [17], ~ 85.5 to ~ 90% by binder jetting [15, 42], and ~ 83.4 to ~ 90.9% by extrusion 3D printing [27, 43–46]. Moreover, the relative density of the present study is close to the ones obtained with the MIM process [47–49], i.e., 91.2 to 96.4 % and the data sheet of MIM feedstock [50], i.e., ≥ 95.7%.

The overall optimized process aims to achieve high density, and it opens the way to the fabrication of pure copper customized parts with high density and minimum surface roughness which are difficult to fabricate with other 3D printing methods. The process saves the cost and time of die preparation for the MIM process of copper, and it can be used to fabricate parts at batch production by obtaining professional accuracy. Therefore, the present methodology should allow fabricating pure copper customized parts such as complex-shaped electric discharge machining electrodes for customized machining of hard material, optimized shape heat sink for better heat dissipation in power electronics, ordered foam structures with low weight for heat exchangers, and parts with internal cooling channels like bearing, dies. The complex shapes fabricated by the present study process could result in homogenous density in the overall structure. However, density could vary in thin features of complex shapes, which is the future interest of the authors to explore. Also, the present work can be explored for another market available MIM material.

**Supplementary Information** The online version contains supplementary material available at https://doi.org/10.1007/s00170-021-07188-y.

**Authors' contributions** Gurminder Singh: conceptualization, methodology, investigation, software, writing–original draft preparation. Jean-Michel Missiaen: conceptualization, supervision, validation, writing–reviewing and editing. Didier Bouvard: supervision, visualization, writing–reviewing and editing. Jean-Marc Chaix: supervision, resources, writing–reviewing and editing. All authors read and approved the final manuscript.

**Funding** Open Access funding provided by the IReL Consortium. The authors thank the Institute Carnot Energies du Future and Labex CEMAM for their significant contribution to the funding of this work.

**Data availability** Not applicable

**Code availability** Not applicable

## Declarations

**Conflicts of interest** The authors declare that they have no conflict of interest.

## References


1. Nazir A, Abate KM, Kumar A, Jeng JY (2019) A state-of-the-art review on types, design, optimization, and additive manufacturing of cellular structures. Int J Adv Manuf Technol 104:3489–3510. https://doi.org/10.1007/s00170-019-04085-3
2. Zimmermann M, Müller D, Kirsch B, Greco S, Aurich JC (2020) Analysis of the machinability when milling AlSi10Mg additively manufactured via laser-based powder bed fusion. Int J Adv Manuf Technol 112:989–1005. https://doi.org/10.1007/s00170-020-06391-7
3. Jiang J, Weng F, Gao S, Stringer J, Xu X, Guo P (2019) A support interface method for easy part removal in directed energy deposition. Manuf Lett 20:30–33. https://doi.org/10.1016/j.mfglet.2019.04.002
4. Singh S, Singh G, Prakash C, Ramakrishna S (2020) Current status and future directions of fused fi lament fabrication. J Manuf Process 55:288–306. https://doi.org/10.1016/j.jmapro.2020.04.049
5. Singh S, Ramakrishna S, Singh R (2017) Material issues in additive manufacturing: A review. J Manuf Process 25:185–200. https://doi.org/10.1016/j.jmapro.2016.11.006
6. Al-Tamimi AA, Hernandez MA, Omar A et al (2020) Mechanical, biological and tribological behaviour of fixation plates 3D printed by electron beam and selective laser melting. Int J Adv Manuf Technol 109:673–688. https://doi.org/10.1007/s00170-020-05676-1
7. Ameen W, Al-Ahmari A, Mohammed MK (2019) Self-supporting overhang structures produced by additive manufacturing through electron beam melting. Int J Adv Manuf Technol 104:2215–2232. https://doi.org/10.1007/s00170-019-04007-3
8. Singh R, Singh R, Dureja JS, Farina I, Fabbrocino F (2017) Investigations for dimensional accuracy of Al alloy/Al-MMC developed by combining stir casting and ABS replica based investment casting. Compos Part B Eng 115:203–208. https://doi.org/10.1016/j.compositesb.2016.10.008
9. Singh G, Pandey PM (2020) Experimental investigations into mechanical and thermal properties of rapid manufactured copper parts. Proc Inst Mech Eng Part C J Mech Eng Sci 234:82–95. https://doi.org/10.1177/0954406219875483
10. Singh G, Singh S, Singh J, Pandey PM (2020) Parameters effect on electrical conductivity of copper fabricated by rapid manufacturing. Mater Manuf Process 00:1–12. https://doi.org/10.1080/10426914.2020.1784937
11. Hong D, Chou DT, Velikokhatnyi OI, Roy A, Lee B, Swink I, Issaev I, Kuhn HA, Kumta PN (2016) Binder-jetting 3D printing and alloy development of new biodegradable Fe-Mn-Ca/Mg alloys. Acta Biomater 45:375–386. https://doi.org/10.1016/j.actbio.2016.08.032
12. Chantzis D, Liu X, Politis DJ, el Fakir O, Chua TY, Shi Z, Wang L (2020) Review on additive manufacturing of tooling for hot stamping. Int J Adv Manuf Technol 109:87–107. https://doi.org/10.1007/s00170-020-05622-1
13. Singh J, Singh G, Pandey PM (2020) Electric discharge machining using rapid manufactured complex shape copper electrode: Parametric analysis and process optimization for material removal rate, electrode wear rate and cavity dimensions. Proc Inst Mech Eng Part C J Mech Eng Sci 0:1–15. https://doi.org/10.1177/0954406220906445, 234
14. Bourell DLD, Beaman JJ, Leu MC, Rosen DW (2009) A brief history of additive manufacturing and the 2009 roadmap for additive manufacturing: looking back and looking ahead. US – TURKEY Work Rapid Technol 1:5–11. https://doi.org/10.1089/3dp.2013.0002
15. Bai Y, Williams CB (2015) an Exploration of Binder Jetting of Copper. Rapid Prototyp J 21:177–185. https://doi.org/10.1108/RPJ-12-2014-0180
16. Singh G, Pandey PM (2020) Rapid manufacturing of copper-graphene composites using a novel rapid tooling technique. Rapid Prototyp J 26:765–776. https://doi.org/10.1108/RPJ-10-2019-0258
17. Singh G, Pandey PM (2019) Rapid manufacturing of copper components using 3D printing and ultrasonic assisted pressureless sintering: experimental investigations and process optimization. J Manuf Process 43:253–269. https://doi.org/10.1016/j.jmapro.2019.05.010
18. Singh G, Pandey PM (2019) Uniform and graded copper open cell ordered foams fabricated by rapid manufacturing: surface morphology, mechanical properties and energy absorption capacity. Mater Sci Eng A 761:138035. https://doi.org/10.1016/j.msea.2019.138035
19. Godec D, Cano S, Holzer C, Gonzalez-Gutierrez J (2020) Optimization of the 3D printing parameters for tensile properties of specimens produced by fused filament fabrication of 17-4PH stainless steel. Materials (Basel) 13:. https://doi.org/10.3390/ma13030774
20. Rane K, Cataldo S, Parenti P et al (2018) Rapid Production of Hollow SS316 Profiles by Extrusion based Additive Manufacturing. 140014. https://doi.org/10.1063/1.5035006
21. Rane K, Di Landro L, Strano M (2019) Processability of SS316L powder - binder mixtures for vertical extrusion and deposition on table tests. Powder Technol 345:553–562. https://doi.org/10.1016/j.powtec.2019.01.010
22. Kukla C, Cano S, Kaylani D, Schuschnigg S, Holzer C, Gonzalez-Gutierrez J (2019) Debinding behaviour of feedstock for material extrusion additive manufacturing of zirconia. Powder Metall 62:196–204. https://doi.org/10.1080/00325899.2019.1616139
23. Rane K, Farid MA, Hassan W, Strano M (2021) Effect of printing parameters on mechanical properties of extrusion-based additively manufactured ceramic parts. Ceram Int 1–10. https://doi.org/10.1016/j.ceramint.2021.01.066
24. Rane K, Petrò S, Strano M (2020) Evolution of porosity and geometrical quality through the ceramic extrusion additive manufacturing process stages. Addit Manuf 32:101038. https://doi.org/10.1016/j.addma.2020.101038
25. Hong S, Sanchez C, Du H, Kim N (2015) Fabrication of 3D printed metal structures by use of high-viscosity Cu paste and a screw extruder. J Electron Mater 44:836–841. https://doi.org/10.1007/s11664-014-3601-8
26. Yan X, Hao L, Xiong W, Tang D (2017) Research on influencing factors and its optimization of metal powder injection molding without mold via an innovative 3D printing method. RSC Adv 7:55232–55239. https://doi.org/10.1039/c7ra11271h
27. Zhao Y, Gao W, Xi J, Li H, Ren F (2020) Development of copper powder paste for direct printing and soft mold casting. Addit Manuf 31:100992. https://doi.org/10.1016/j.addma.2019.100992
28. Ren L, Zhou X, Song Z, Zhao C, Liu Q, Xue J, Li X (2017) Process parameter optimization of extrusion-based 3D metal printing utilizing PW-LDPE-SA binder system. Materials (Basel) 10 https://doi.org/10.3390/ma10030305
29. Singh G, Missiaen JM, Bouvard D, Chaix JM (2021) Copper extrusion 3D printing using metal injection moulding feedstock: analysis of process parameters for green density and surface roughness optimization. Addit Manuf 38:101778. https://doi.org/10.1016/j.addma.2020.101778
30. Ott J, Burghardt A, Britz D, Mucklich F (2019) Free-sintering study of pressure-less manufactured green bodies made of fine Cu powder for electronic applications. In: Euro PM2019 International Powder Metallurgy Congress & Exhibition. Netherlands
31. German R (2014) Sintering: from empirical observations to scientific principles

32. Olmos L, Bouvard D, Salvo L, Bellet D, di Michiel M (2014) Characterization of the swelling during sintering of uniaxially pressed copper powders by in situ X-ray microtomography. J Mater Sci 49:4225–4235. https://doi.org/10.1007/s10853-014-8117-3
33. Zhou X, Dai N, Chu M, Wang L, Li D, Zhou L, Cheng X (2020) X-ray CT analysis of the influence of process on defect in Ti-6Al-4V parts produced with Selective Laser Melting technology. Int J Adv Manuf Technol 106:3–14. https://doi.org/10.1007/s00170-019-04347-0
34. Boulos V, Fristot V, Houzet D, et al (2012) Investigating performance variations of an optimized GPU-ported granulometry algorithm To cite this version : HAL Id : hal-00787861 Investigating performance variations of an optimized GPU-ported granulometry algorithm. In: Design and Architectures for Signal and Image Processing (DASIP). pp 1–6
35. Jiang J, Xu X, Stringer J (2018) Support Structures for Additive Manufacturing: A Review. J Manuf Mater Process 2:64. https://doi.org/10.3390/jmmp2040064
36. Zaky MT (2004) Effect of solvent debinding variables on the shape maintenance of green molded bodies. J Mater Sci 39:3397–3402
37. Li Y, Liu S, Qu X, Huang B (2003) Thermal debinding processing of 316L stainless steel powder injection molding compacts. J Mater Process Technol 137:65–69. https://doi.org/10.1016/S0924-0136(02)01067-1
38. Thompson Y, Gonzalez-Gutierrez J, Kukla C, Felfer P (2019) Fused filament fabrication, debinding and sintering as a low cost additive manufacturing method of 316L stainless steel. Addit Manuf 30:100861. https://doi.org/10.1016/j.addma.2019.100861
39. Mohsin IU, Lager D, Gierl C et al (2011) Simulation and optimisation for thermal debinding of copper MIM parts using thermokinetic analysis simulation and optimisation for thermal debinding of copper MIM parts using thermokinetic analysis. Powder Metall 54:30–35. https://doi.org/10.1179/003258910X12740974839620
40. Tang Y, Zhou R, Li H, Yuan W, Lu L (2014) Experimental study on the tensile strength of a sintered porous metal composite. Mater Sci Eng A 607:536–541. https://doi.org/10.1016/j.msea.2014.04.039
41. Zhu Y, Wu Z, Hartley WD, Sietins JM, Williams CB, Yu HZ (2020) Unraveling pore evolution in post-processing of binder jetting materials: X- ray computed tomography , computer vision , and machine learning. Addit Manuf 34:101183. https://doi.org/10.1016/j.addma.2020.101183
42. Bai Y, Wagner G, Williams CB (2017) Effect of particle size distribution on powder packing and sintering in binder jetting additive manufacturing of metals. J Manuf Sci Eng 139:1–6. https://doi.org/10.1115/1.4036640
43. Ecker JV, Dobrezberger K, Gonzalez-Gutierrez J, Spoerk M, Gierl-Mayer C, Danninger H (2020) Additive manufacturing of steel and copper using fused layer modelling: material and process development. Powder Metall Prog 19:63–81. https://doi.org/10.1515/pmp-2019-0007
44. Leyh C, Martin S, Schaffer T (2017) Industry 4.0 and Lean production-a matching relationship? An analysis of selected Industry 4.0 models. Proc 2017 Fed Conf Comput Sci Inf Syst FedCSIS 2017(11):989–993. https://doi.org/10.15439/2017F365
45. Ren L, Zhou X, Song Z, Zhao C, Liu Q, Xue J, Li X (2017) Process parameter optimization of extrusion-based 3D metal printing utilizing PW-LDPE-SA binder system. Materials (Basel) 10. https://doi.org/10.3390/ma10030305
46. Yan X, Wang C, Xiong W, Hou T, Hao L, Tang D (2018) Thermal debinding mass transfer mechanism and dynamics of copper green parts fabricated by an innovative 3D printing method. RSC Adv 8:10355–10360. https://doi.org/10.1039/c7ra13149f
47. Moballegh L, Morshedian J, Esfandeh M (2005) Copper injection molding using a thermoplastic binder based on paraffin wax. 59:2832–2837. https://doi.org/10.1016/j.matlet.2005.04.027
48. Muhsan AS, Ahmad F, Mohamed NM et al (2013) Uniform dispersion of multiwalled carbon nanotubes in copper matrix nanocomposites using metal injection molding technique. Int J Manuf Eng 2013:1–9
49. Johnson JL, Tan LK, Bollina R, Suri P, German RM (2013) Evaluation of copper powders for processing heat sinks by metal injection moulding 48:5899:. https://doi.org/10.1179/003258905X37792
50. GmbH P (2011) data sheet - polyMIM ® Cu999 (80057)